UNITED STATES DEPARTMENT OF THE INTERIOR

GEOLOGICAL SURVEY

A Model for Creeping Flow in Landslides

By

W. Z. Savage and A. F. Chleborad

Open-File Report 81-124

1981

Contents

Illustrations

A Model for Creeping Flow in Landslides

by W. Z. Savage and A. F. Chleborad

Introduction

Models of slow, steady creeping flow in landslides have been presented by Ter-Stepanian (1963) and Yen (1969). Both authors modeled the creeping flow by considering the flow under gravity of a Bingham or viscoplastic substance on an infinitely long slope.

A similar model will be considered in what follows. However, instead of the two-dimensional Coulomb failure criterion used by Ter-Stepanian (1963) and Yen (1969) the three-dimensional generalization of this criterion (Drucker and Prager, 1952) will be invoked. This leads to the definition of a Bingham substance similar to that given by Olszak and Perzyna (1966).

The creeping flow being considered here occurs at depth in a nearly planar landslide in response to gravity, in contrast to the more localized surface creep that occurs in response to such factors as freezing and thawing cycles. The model developed here will be applied to the case histories described by Ter-Stepanian (1963) and Yen (1969) and to Chleborad's (1980) field results.

Bingham Substance

A Bingham substance has the property that below a certain stress--called the yield stress--it behaves elastically. Above the yield stress it behaves viscoplastically. Specifically, we have the constitutive equations;

$$\sigma_{ij}' = 2\mu e_{ij}' \text{ when } \tfrac{1}{2}\sigma_{ij}'\sigma_{ij}' \leq [k-\alpha J_1]^2, \tag{1}$$

$$\sigma_{ij}' = 2\eta\varepsilon_{ij}' \text{ when } \tfrac{1}{2}\sigma_{ij}'\sigma_{ij}' > [k-\alpha J_1]^2, \tag{2}$$

where η is the nonlinear viscosity

$$\eta = \eta_1 + [k-\alpha J_1](2\varepsilon_{ij}'\varepsilon_{ij}')^{-\frac{1}{2}} \tag{3}$$

The constant μ is the elastic shear modulus and η_1 is the viscosity. Primes indicate deviatoric stresses and strains, and ε_{ij}' indicates deviatoric strain rates. The product $\tfrac{1}{2}\sigma_{ij}'\sigma_{ij}'$ is the second invariant of the stress deviation. The strains are defined by $e_{ij} = \tfrac{1}{2}\left[\frac{\partial u_i}{\partial x_j} + \frac{\partial u_j}{\partial x_i}\right]$ where u_i represents particle displacements.

The strain rates are given by $\varepsilon_{ij} = \tfrac{1}{2}\left[\frac{\partial v_i}{\partial x_j} + \frac{\partial v_j}{\partial x_i}\right]$ where v_i are the particle velocities. The constants k and α are positive at each point in the material, and $J_1 = \sigma_{ii}$ is the first invariant of the stress tensor. The constants k and α are related to the cohesion c and the angle of internal friction ϕ determined from triaxial tests by $\alpha = \frac{2\sin\phi}{\sqrt{3}(3+\sin\phi)}$ and by $k = \frac{6c\cos\phi}{\sqrt{3}(3+\sin\phi)}$ (see Corp and others, 1975).

Equations 1 and 2 are the same as those given by Oldroyd (1947) for a Bingham substance, except that the pressure-dependent yield function defined by Drucker and Prager (1952) is included here, that is, we include αJ_1 in the definition of yielding.

As a special case, consider simple shear when all shear stresses except $\sigma_{12}=\sigma_{21}$ vanish. For no confining pressure we have $\sigma_{11}=\sigma_{22}=\sigma_{33}=\sigma_{13}=\sigma_{23}=0$ and equations 1 and 2 become

$$\sigma_{12} = \mu \frac{\partial u_1}{\partial x_2} \qquad \sigma_{12}^2 \leq k^2, \tag{4}$$

$$\sigma_{12} = \eta_1 \frac{\partial u_1}{\partial x_2} + k \qquad \sigma_{12}^2 > k, \tag{5}$$

These relations are shown graphically in figure 1. For $\sigma_{12} < k$ the body behaves elastically, that is, the shear strain rate ε_{12} vanishes. For $\sigma_{12} \geq k$ the body behaves viscously and the relation between σ_{12} and ε_{12} is given by equation 5. We see that this relation is the same as that in a Newtonian viscous body except that the shear stress is greater by k. Thus, k is the yield stress in simple shear under zero confining pressure.

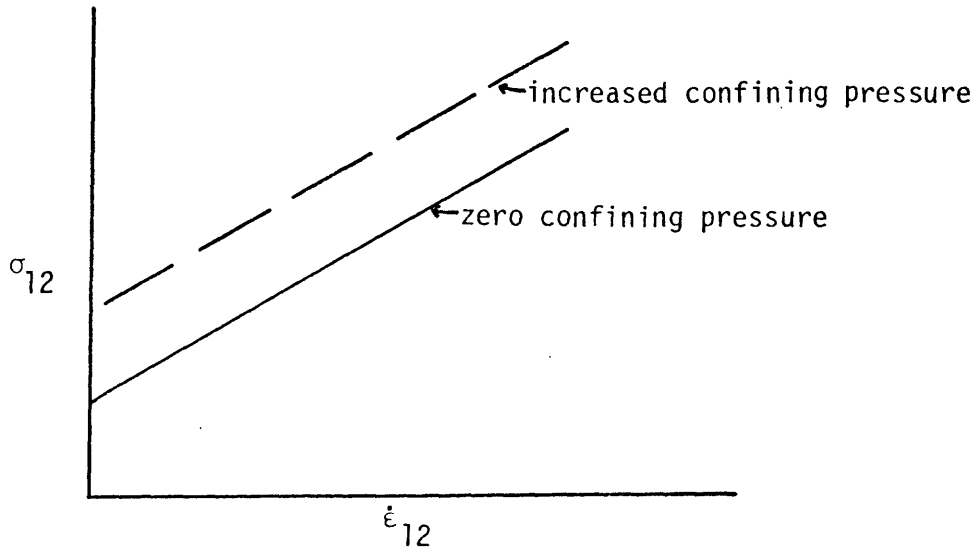

Figure 1.--Behavior of a Bingham body in simple shear.

Now consider the case when a confining pressure $\sigma_{11}=\sigma_{22}=\sigma_{33}=-\sigma$ is superposed on the state of pure shear. Relations 4 and 5 become

$$\sigma_{12} = \mu \frac{\partial u_1}{\partial x_2} \text{ when } \sigma_{12}^2 < [k + 3\alpha\sigma]^2, \tag{6}$$

$$\sigma_{12} = \eta_1 \frac{\partial v_1}{\partial x_2} + k + 3\alpha\sigma \text{ when } \sigma_{12}^2 \geq [k + 3\alpha\sigma]^2, \tag{7}$$

An increase in confining pressure leads to an increase in yield strength of the body. For a given confining pressure the stress-strain rate relation is shown as a dashed line in figure 1.

Returning to equations 1 through 3, clearly these represent a three-dimensional generalization of equations 6 and 7.

Any post-yielding flow of the Bingham substance must satisfy continuity and equilibrium. From equation 2; $\sigma_{ii}' = 2\eta \frac{\partial v_i}{\partial x_i}$, but the first invariant of the stress deviator, $\sigma_{ii}' = 0$, and thus $\frac{\partial v_i}{\partial x_i} = 0$. The equation of continuity is then

$$\varepsilon_{ii} = \frac{\partial v_i}{\partial x_i} = 0, \qquad (8),$$

and the flow is that of an incompressible medium. The equilibrium equation is

$$\rho\left(\frac{\partial v_k}{\partial t} + v_j \frac{\partial v_k}{\partial x_j}\right) = \rho F_k + \frac{\partial \sigma_{jk}}{\partial x_j}, \qquad (9)$$

Substituting equation 2 into 9 and taking account of equation 8 leads to the nonlinear Navier-Stokes equation

$$\rho\left(\frac{\partial v_k}{\partial t} + v_j \frac{\partial v_k}{\partial x_j}\right) = \rho F_k - \frac{\partial \sigma}{\partial x_k} + \eta \frac{\partial^2 v_k}{\partial x_j \partial x_j} + \frac{\partial}{\partial x_j}\left[\left[\frac{k - \alpha J_1}{[2\varepsilon_{ij}'\varepsilon_{ij}']^{1/2}}\right]\varepsilon_{jk}\right]^{\approx}, \qquad (10)$$

which applies when $\frac{1}{2}\sigma_{ij}'\sigma_{ij}' \geq [k - \alpha J_1]^2$.

A Landslide Model

Any landslide model should consider the constitutive equation of the material making up the slide, the slope geometry, and the effect of pore pressure. In this model we consider the landslide to be an infinitely long sheet of Bingham material of thickness h flowing steadily under gravity down a slope of $\theta°$. The configuration is shown in figure 2.

Under these conditions, the downslope velocity v_1, the shear stress σ_{12}, and the normal stress σ_{22} are functions of x_2 only and all other stresses and displacements vanish. The equilibrium equation (equation 9) becomes

$$\frac{\partial \sigma_{12}}{\partial x_2} + \rho g \sin\theta = 0 \ , \tag{11}$$

$$\frac{\partial \sigma_{22}}{\partial x_2} - \frac{\partial p}{\partial x_2} - \rho g \cos\theta = 0 \ , \tag{12}$$

where p is the pore pressure, ρ is dry soil density, and g is gravitational acceleration.

Integrating equations 11 and 12 we have,

$$\sigma_{12} = \rho g(x_2-h) \sin\theta + C_s \ , \tag{13}$$

$$\sigma_{22} = -\rho g(x_2-h)\cos\theta + p - C_n \ , \tag{14},$$

where C_s and C_n represent shear and normal tractions due to a surcharge, and $p=\rho_w g[h_p-x_2]\cos\theta$ with h_p, the piezometric level and ρ_w, water density.

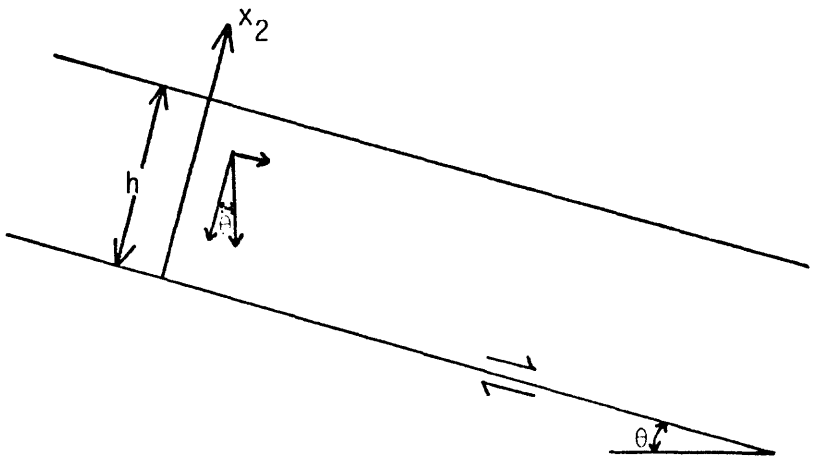

Figure 2.--Infinite sheet of Bingham material under gravity.

Because v_1 is a function of x_2 only, constitutive equation 2 reduces to

$$\sigma_{12} = \eta_1 \frac{\partial v_1}{\partial x_2} + k - 3\alpha\sigma_{22} \ , \qquad (15).$$

Substituting equations 13 and 14 into 15 we have

$$\eta_1 \frac{\partial v_1}{\partial x_2} = \rho g[h-x_2]\sin\theta + C_s - k + 3\alpha[\rho g(x_2-h)\cos\theta + p - C_n] \ , \qquad (16)$$

which describes the velocity gradient in the flow.

When $\sigma_{12} = k + 3\alpha\sigma$, that is, the material is on the point of yielding, we see from equation 15 that the velocity gradient $\frac{\partial v_1}{\partial x_2}$ vanishes. This occurs, as can be seen from equation 16, at a height given by

$$x_2^* = \frac{\rho gh\sin\theta + 3\alpha g(\rho_w h_p - \rho h)\cos\theta - 3\alpha C_n + C_s - k}{\rho g\sin\theta + 3\alpha g(\rho_w - \rho)\cos\theta} \ , \qquad (17).$$

Equation 17 (subtracted from h) defines the depth of a "rigid" plug. For $x_2^* < x_2 \leq h$ the shear strain rate vanishes and the material behaves elastically. Because the elastic strains in the plug are small relative to strains in the underlying viscoplastic material, we can say that the overlying material is rigid, that is, μ, the shear modulus in equation 1 is taken to be infinite.

Equation 16 is next integrated to give the distribution of velocity in the viscoplastic layer extending from $x_2=0$ to $x_2=x_2^*$. At $x_2=0$, $v_1=0$, and thus,

$$v_1=[3\alpha(\rho-\rho_w)g\cos\theta-\rho g\sin\theta]\frac{x_2^2}{2n_1}+[\rho gh\sin\theta+3\alpha g[\rho_w h_p-\rho h]\cos\theta-3\alpha C_n+C_s-k]\frac{x_2}{n_1} \qquad (18).$$

This reaches a maximum at the boundary with the rigid plug at $x_2=x_2^*$. This maximum velocity v_1^* is given by,

$$v_1^*=\frac{[\rho gh\sin\theta+3\alpha g(\rho_w h_p-\rho h)\cos\theta-3\alpha C_n+C_s-k]^2}{2n_1[\rho g\sin\theta+3\alpha g(\rho_w-\rho]\cos\theta]}, \qquad (19).$$

For $x_2^*\leq x_2\leq h$ the rigid plug moves with the velocity v_1^*. Note that by using the definitions of x_2^* and v_1^* in equation 18 the distribution of velocity in the viscoplastic layer may be written as,

$$v_1=v_1^*\left[\frac{2x_2^*-x_2}{x_2^*}\right]x_2, \text{ for } 0\leq x_2\leq x_2^* \qquad (20).$$

Equation 20 shown in figure 3 for various values of x_2^* describes a parabolic velocity distribution with a maximum equal to v_1^* at $x_2=x_2^*$.

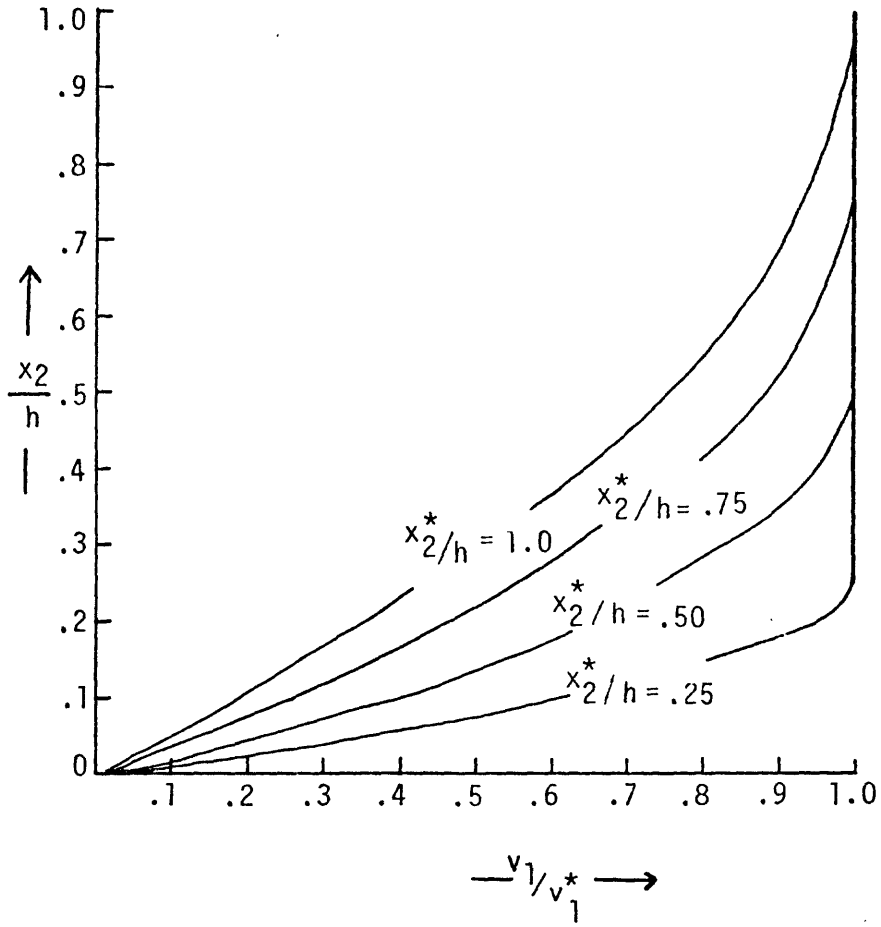

Figure 3.--Velocity profiles for various values of x_2^*/h.

Equations 17 through 20 represent the spectrum of velocity distributions from no flow when $k=\rho ghsin\theta+3\alpha g(\rho_w h_p-\rho h)cos\theta-3\alpha C_n+C_s$ giving $x_2^*=0$ to purely viscous flow when k and α are zero. The maximum velocity (at $x_2=h$) is $v_1^*=[\rho ghsin\theta+C_s]^2/2n_1\rho gsin\theta$ or $v_1^*=\frac{\rho gh^2 sin\theta}{2n_1}$ (when $C_s=0$) in this last case. In general, an increase in the slope angle θ, the thickness h, the piezometric level h_p, or the shear traction C_s, or a decrease in k, α, or normal traction C_n, results in a smaller rigid plug (equation 19) and consequently a greater flow velocity (equation 19). However, an increase in viscosity (equation 19) results in a lower flow velocity for any plug thickness.

In effect, equation 17 can be considered a stability criterion. For example, if one finds that $x_2^* \leq 0$ then the zone of viscoplastic flow will vanish and no depth creep will occur. This, of course, does not preclude surface creep which is not considered in this analysis.

Finally, the model presented here is in many respects similar to those of Ter-Stepanian (1963) and Yen (1969). However, it has the advantage of both generality (by being derived from a three-dimensional constitutive law with explicit inclusion of the effects of pore pressure) and mathematical simplicity.

Applications

The model for depth creep developed above is now applied to the examples described by Ter-Stepanian (1965), Yen (1969), and Chleborad (1980). This application will be followed by a brief discussion in which the results will be compared and recommendations for future applications of the theory will be made.

Displacements measured in a creep well in a landslide on the Black Sea coast of the Caucasus (Ter-Stepanian, 1965) are shown in figure 4. Velocities inferred from the displacements that occurred over a period of $4.9X10^7$ s are shown as a solid line in figure 5. Ter-Stepanian takes the height of the zone of creeping flow, x_2^*, to be 2.10 m, the height of the piezometric level is 1.5 m, and the slide thickness, h, is 3.5 m. The slide occurs in a weathered gray argillite on a slope of 23°. The argillite has an angle of internal friction, ϕ=21.17°, a dry density estimated to be 1700 kg/m^3, and a residual cohesion taken to be zero (Yen, 1969). With these values, the predicted height of the rigid plug (equation 17) is 2.1 m and the predicted maximum velocity, v_1^*, (equation 19) is $3.1X10^{-9}$ m/s if the Bingham viscosity, n_1, is assumed to be $2.78X10^{12}$ Ns/m^2. Note that this viscosity differs from Ter-Stepanian's theoretical estimate of $1.29X10^{12}$ Ns/m^2 derived from his equation for depth creep. Finally, the velocity profile predicted by equation 20 after inserting the results from equations 17 and 19 is shown as a dotted line in figure 5.

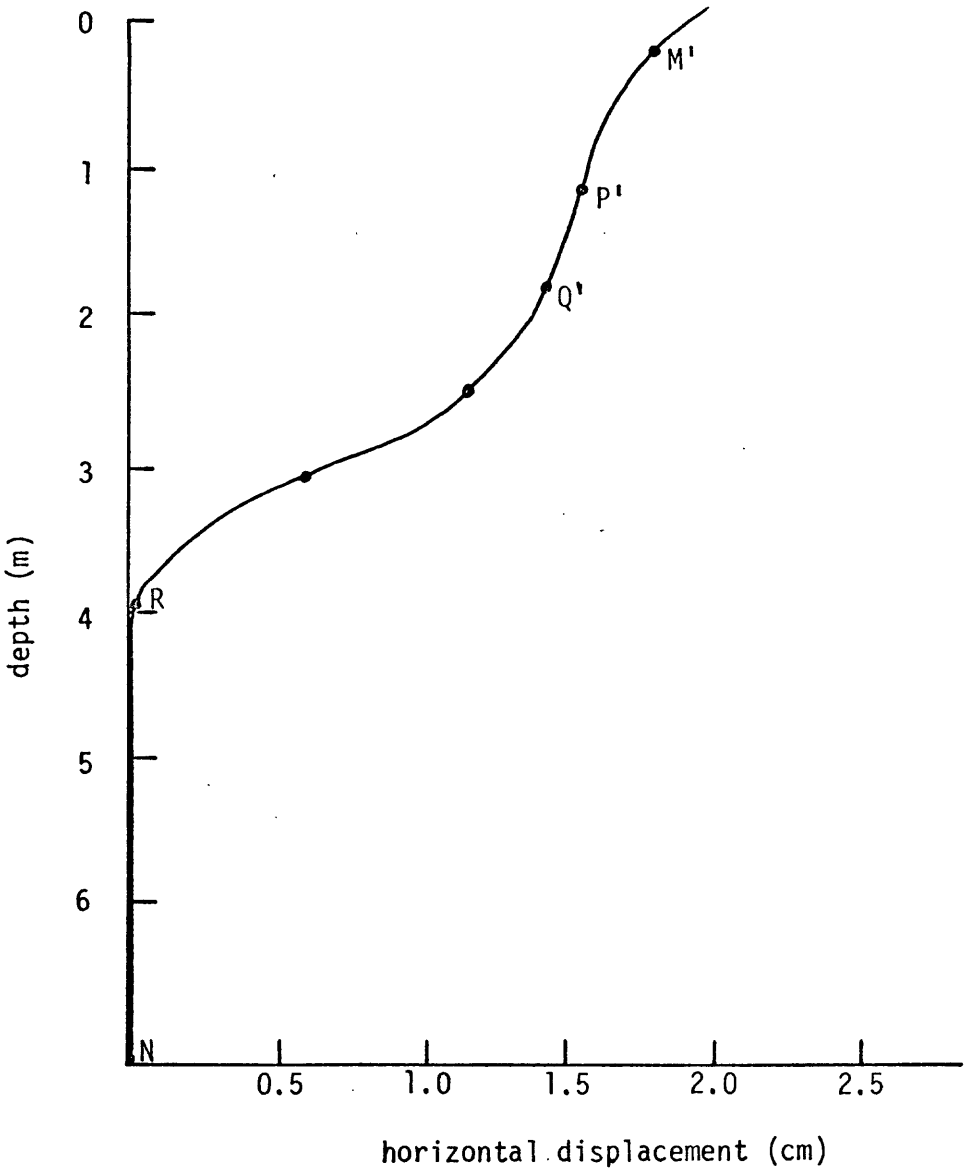

Figure 4.--Creep-deformation profile for landslide slopes of the Black Sea coast of the Caucasus (Ter-Stepanian, 1965). The distance from Q' to M' is taken by Ter-Stepanian (1965) as the "rigid plug", and the distance P' to M' represents a zone of localized surface creep.

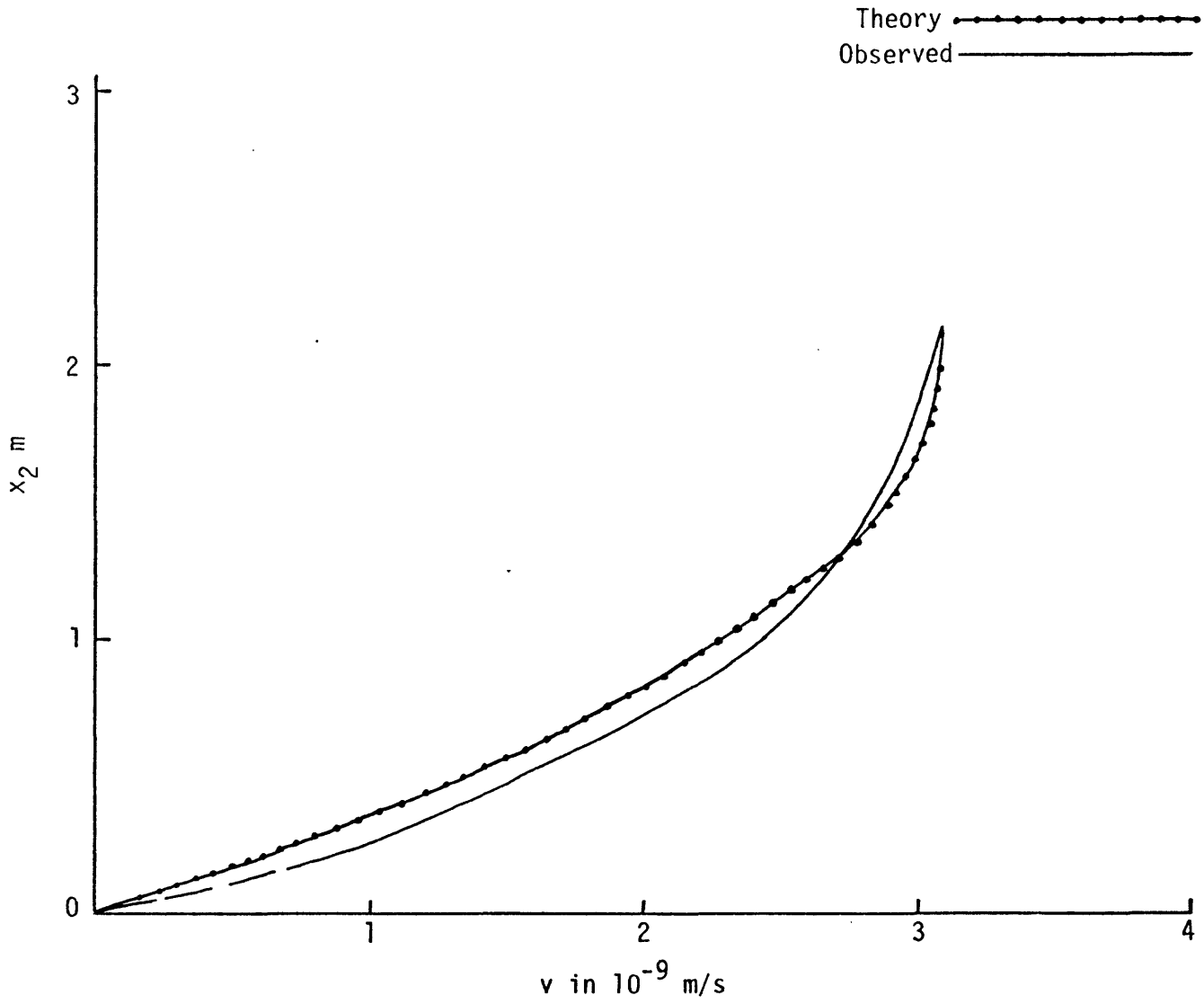

Figure 5.--Comparison between the velocity profile inferred from displacements measured below the zone of surface creep for a slide on the Caucasus Coast of the Black Sea (Ter-Stepanian,1965) and the velocity profile predicted by equations 17 through 20.

Velocities inferred for a slope undergoing creep deformation for a period of $1.89X10^7$ s in coastal southern California (Gould, 1960; Yen, 1969) are compared with those predicted by equations 17 through 20 in figure 6. The creep occurs in a silty clay shale that has a residual angle of friction of 11°-12° and a residual cohesion estimated to be $1.5X10^4$ N/m^2 (Gould, 1960; Yen, 1969). The dry density is 1442 kg/m^3 (Yen, 1969) and the material is creeping on a slope of 13°. Also h=10 m, h_p=8.4 m and the observed height of the zone of creeping flow x_2^* is 1.52 m. If the above values are used in equation 17, the predicted value for x_2^* is 1.52 and if a viscosity of $5.37X10^{11}$ Ns/m^2 is assumed in equation 19, the observed value for the maximum velocity, $4.95X10^{-9}$ m/s, is obtained.

Figure 7 shows a cross section of a shallow landslide near Sheridan, Wyo. (Chleborad, 1980), which we will refer to as the Springer Ranch landslide. Also in figure 7 is an inset showing the location of inclinometer holes for which the cumulative displacements are shown in figures 8 through 12. Figures 13 through 17 show the velocities inferred from the inclinometer data (for a period of $5X10^7$ s) as solid lines and the velocities in the zone of deep creep predicted by equations 17 through 20 for each station.

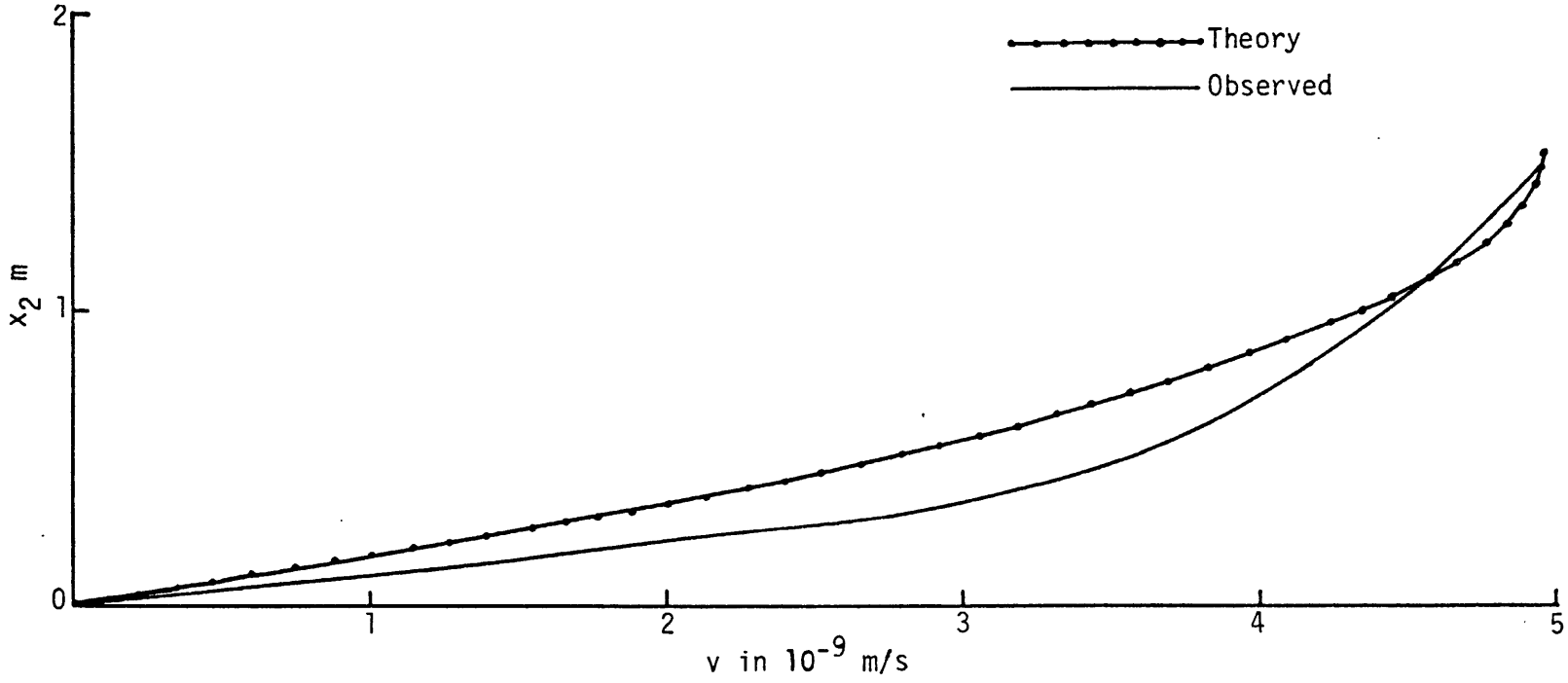

Figure 6.--Comparison between the velocity profile inferred from displacements measured in a slide on the Southern California coast (Yen, 1969) and the velocity profile predicted by equations 17 through 20.

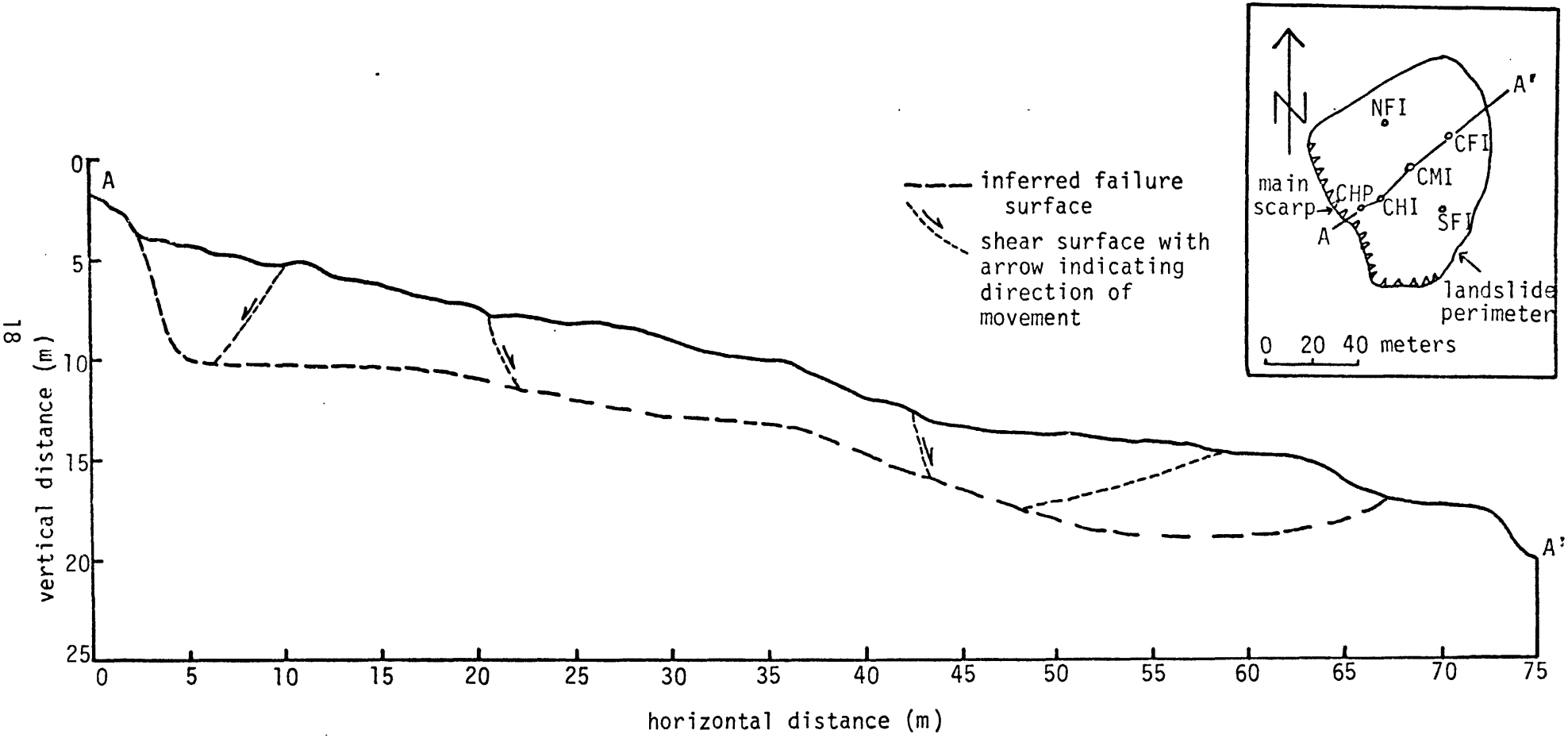

Figure 7.--Landslide cross section showing inferred failure surface and shear surfaces. Drillhole diameters on the plan view are exaggerated for the purpose of illustration. Inset shows line of section A - A' and location of inclinometer holes.

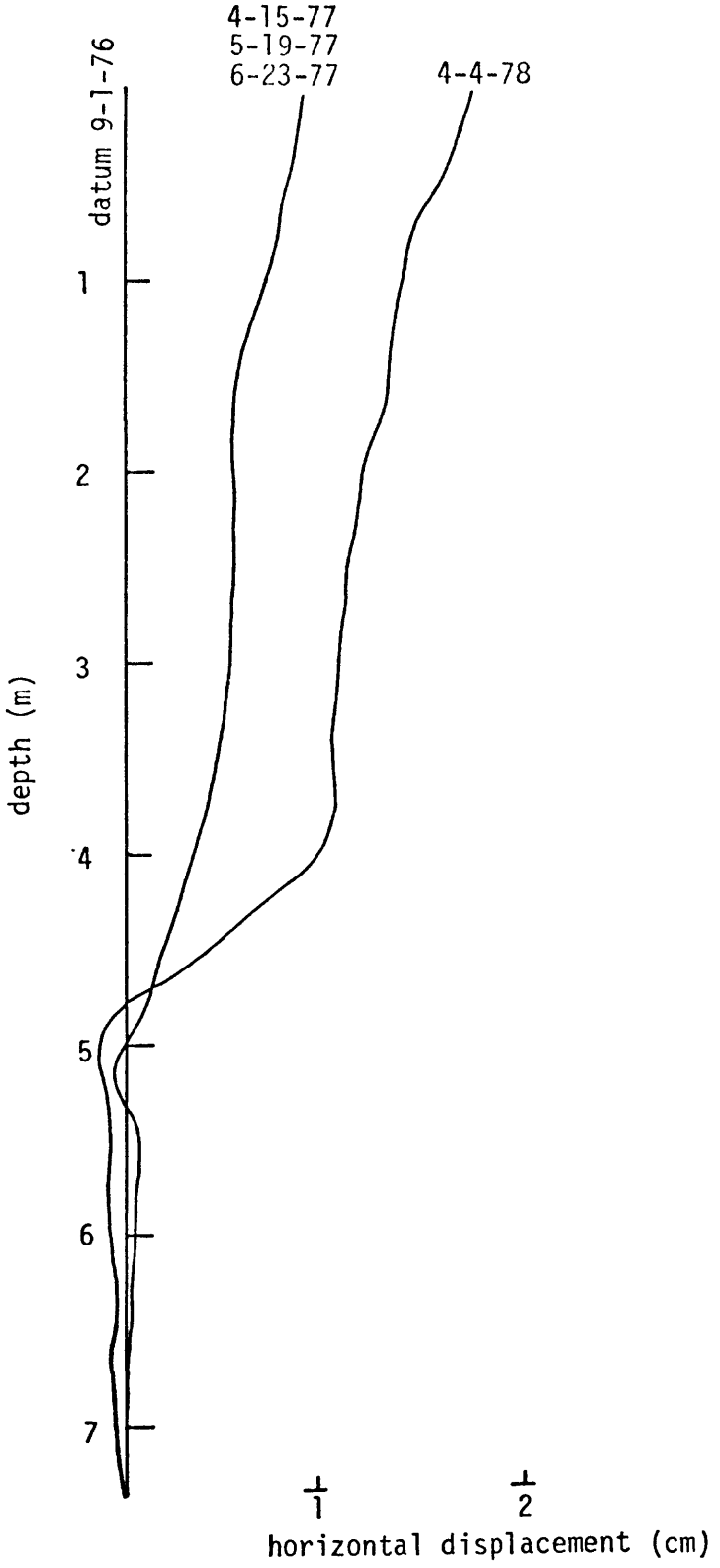

Figure 8.--Cumulative displacement-depth profiles for the center-head inclinometer hole (CHI).

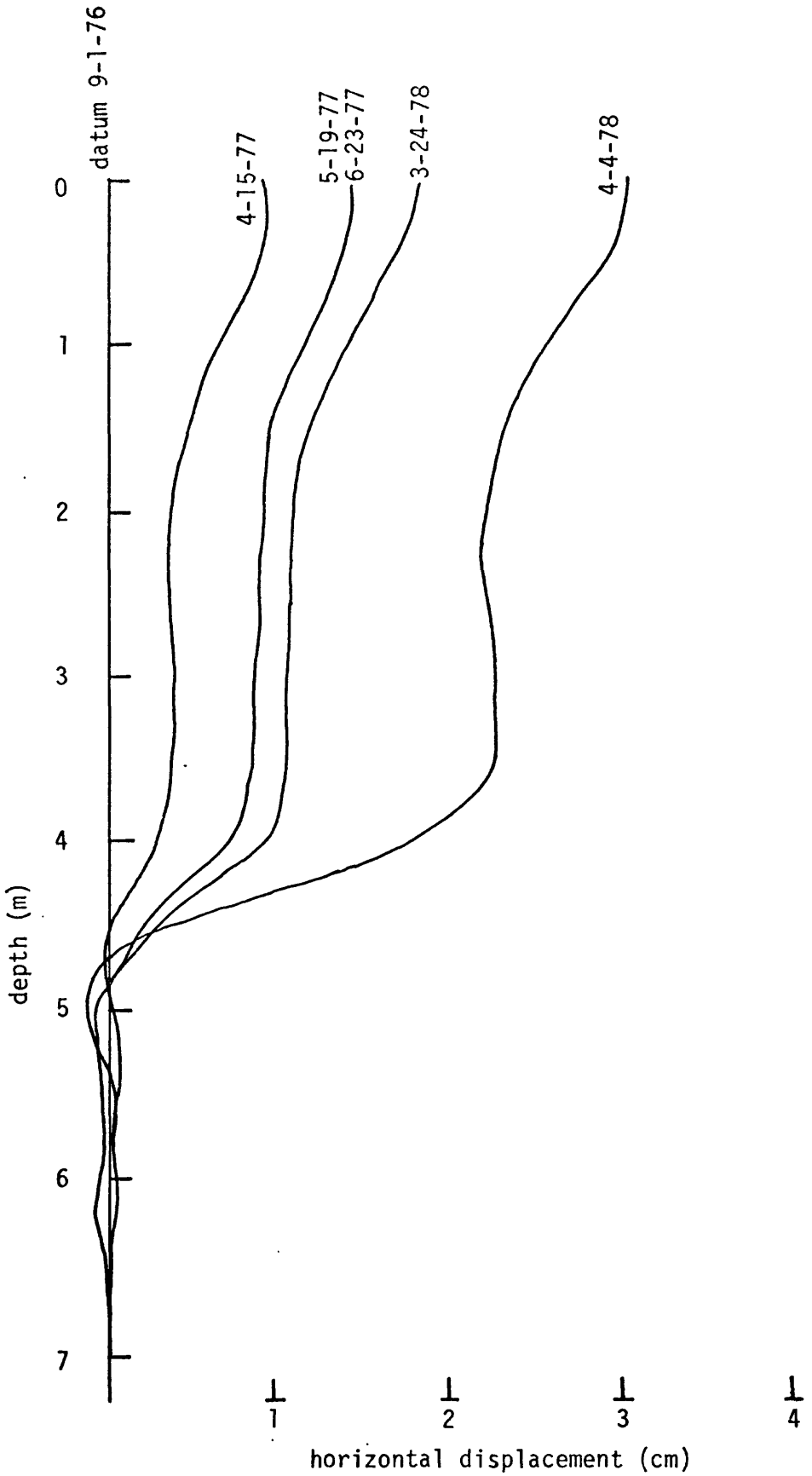

Figure 9.--Cumulative displacement-depth profiles for the north-flank inclinometer hole (NFI).

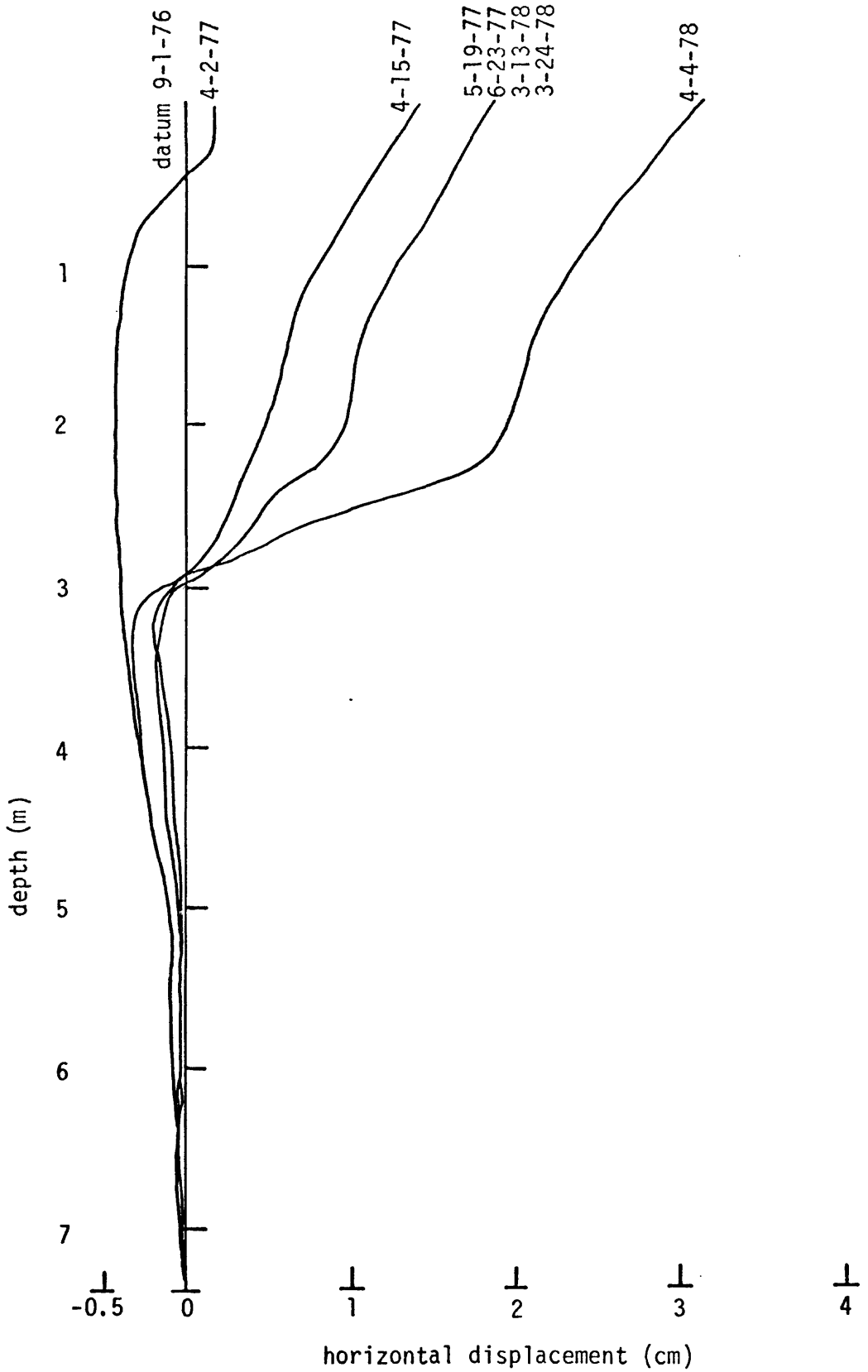

Figure 10.--Cumulative displacement-depth profiles for the center-middle inclinometer hole (CMI).

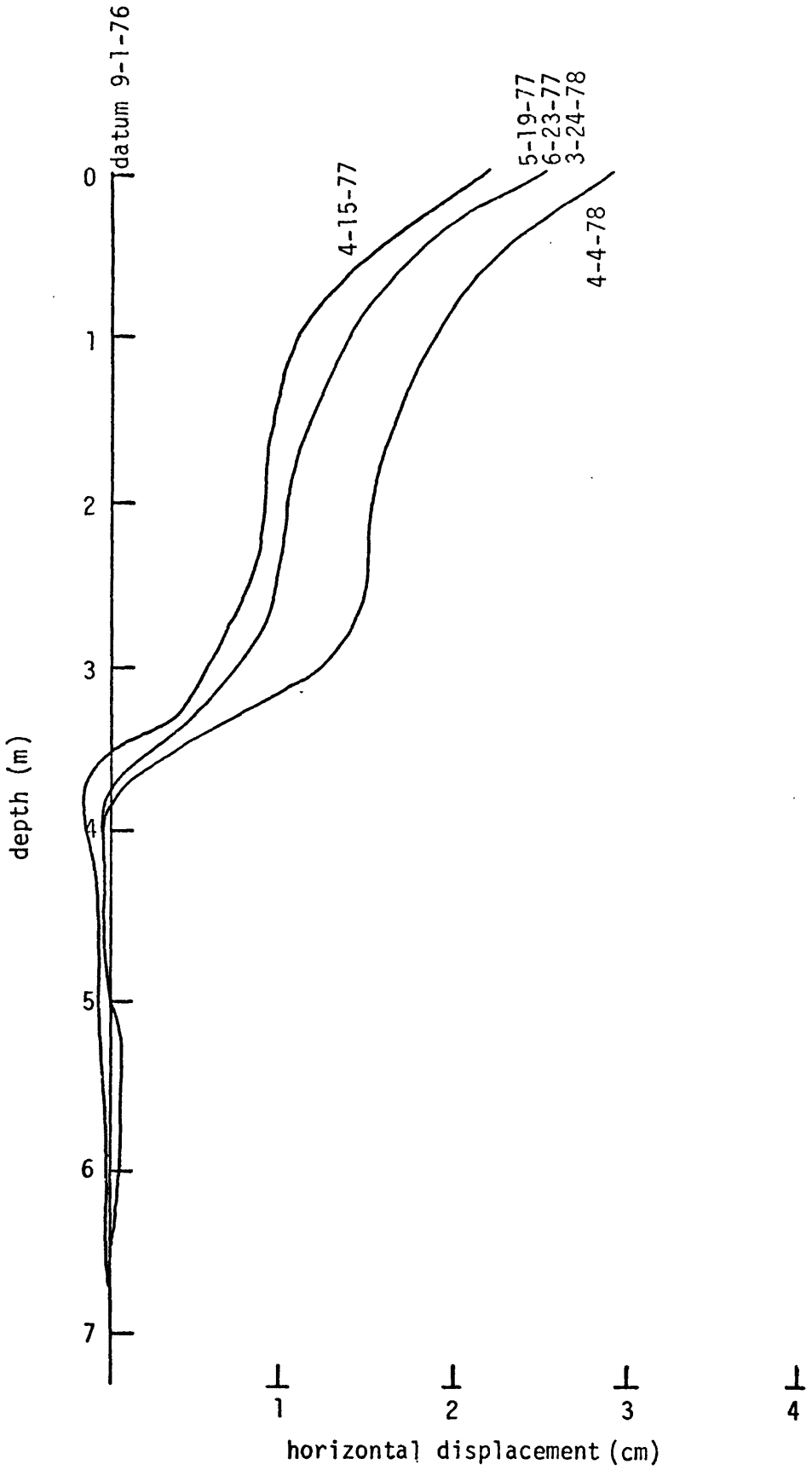

Figure 11--Cumulative displacement-depth profiles for the south-flank inclinometer hole (SFI).

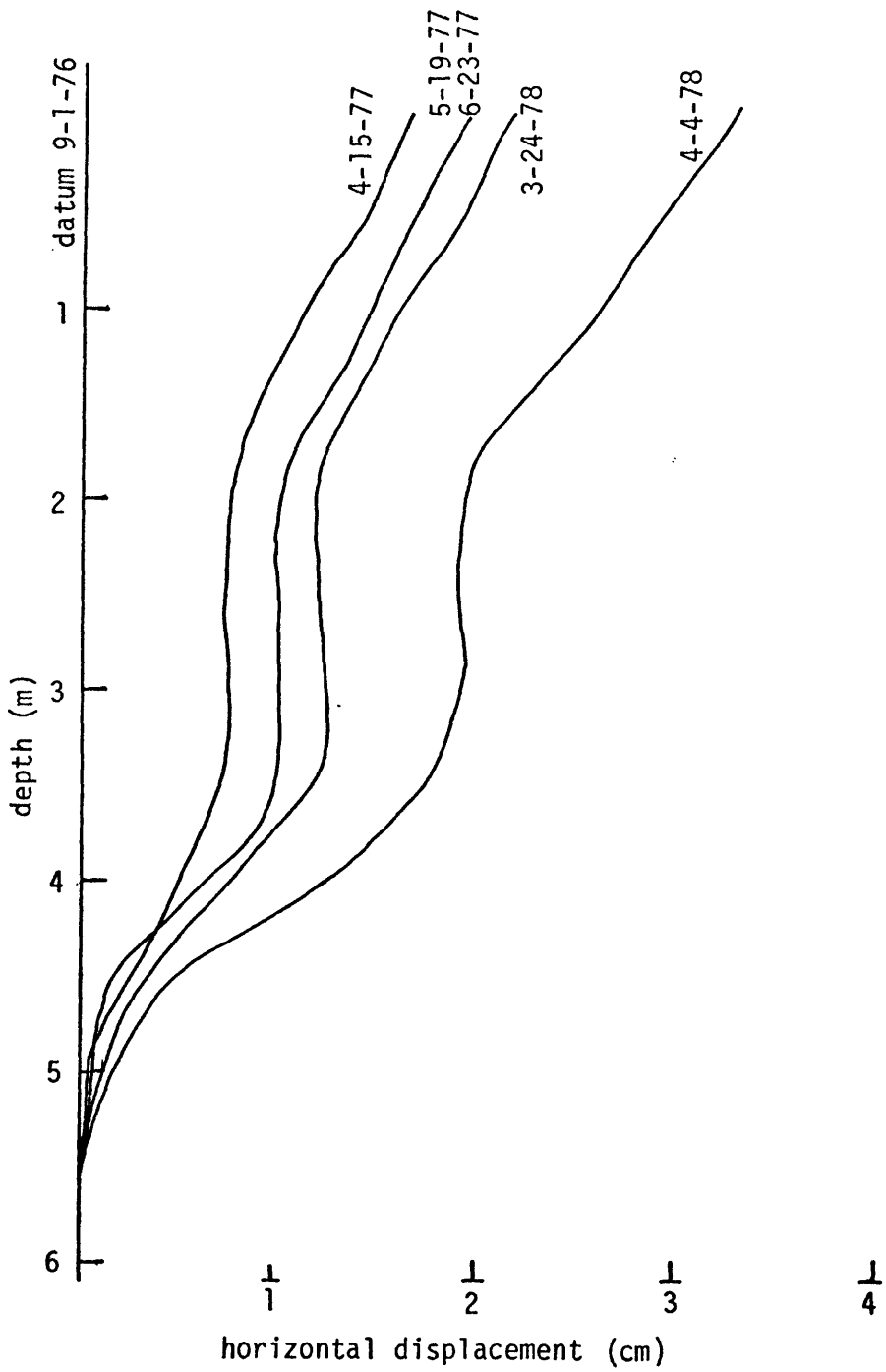

Figure 12.--Cumulative displacement-depth profiles for the center-foot inclinometer hole (CFI).

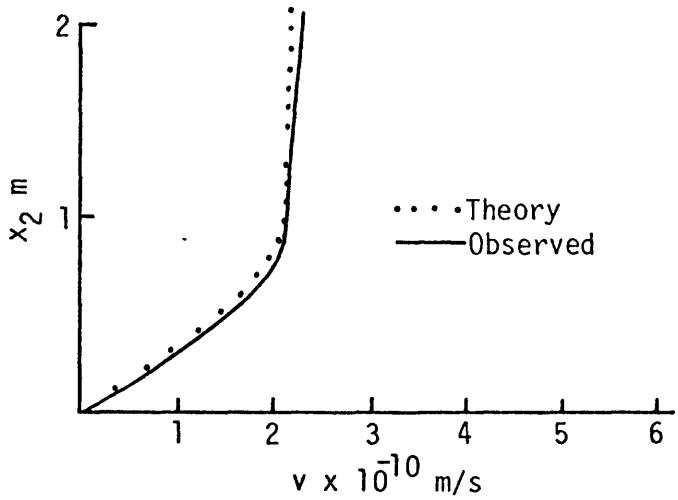

Figure 13.--Measured velocity profile versus theoretical velocity profile for the center-head inclinometer (CHI), Springer Ranch Landslide.

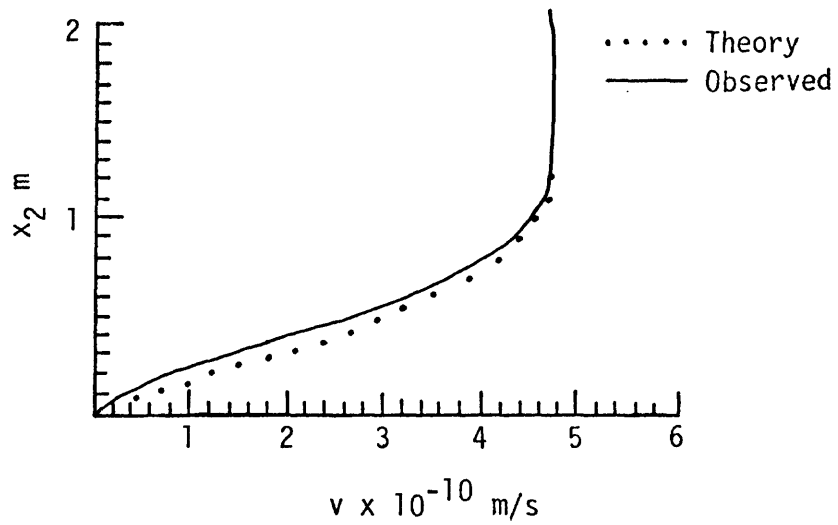

Figure 14.--Measured velocity profile versus theoretical velocity profile for the north-flank inclinometer (NFI), Springer Ranch Landslide.

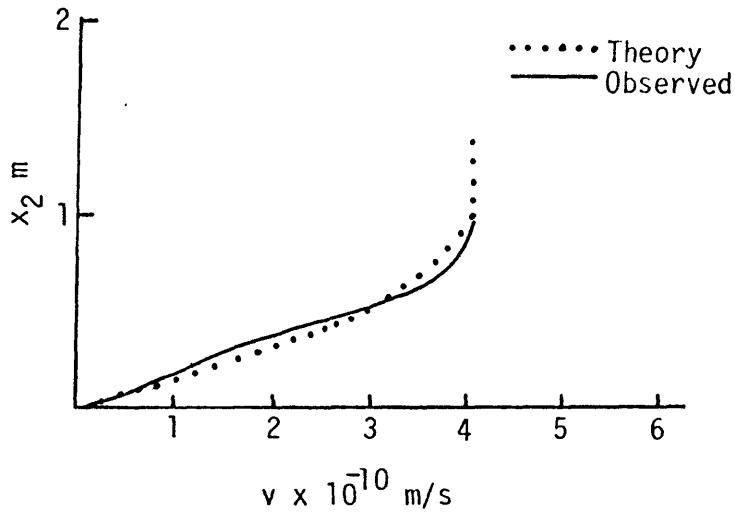

Figure 15.--Measured velocity profile versus theoretical velocity profile for the center-middle inclinometer (CMI), Springer Ranch Landslide.

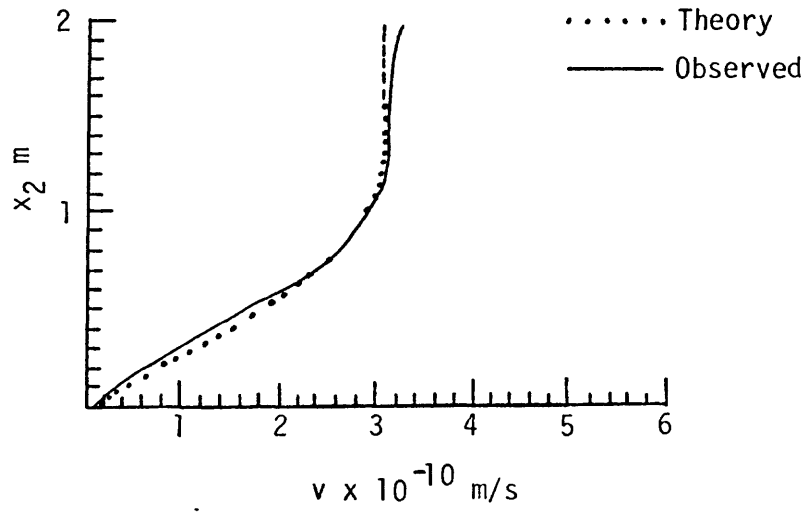

Figure 16.--Measured velocity profile versus theoretical velocity profile for the south-flank inclinometer (SFI), Springer Ranch Landslide.

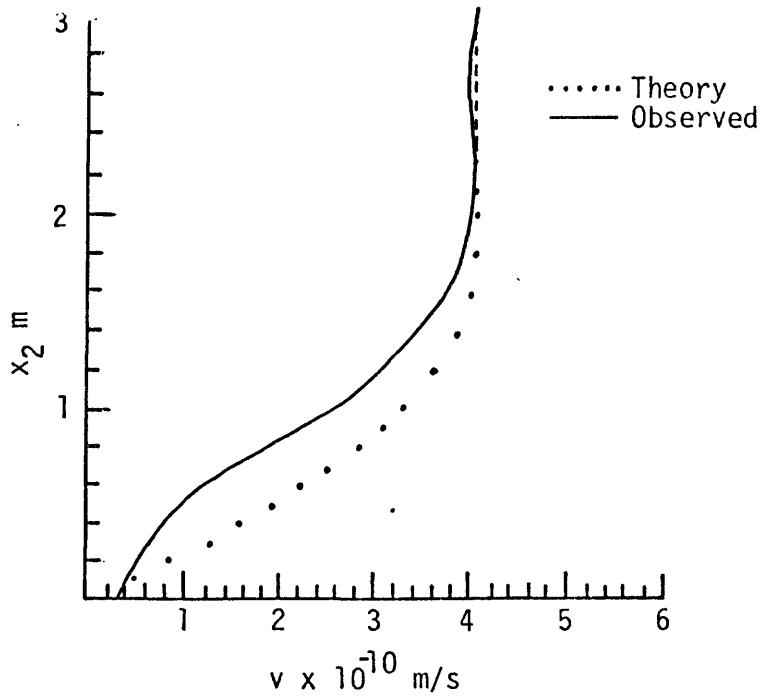

Figure 17.--Measured velocity profile versus theoretical velocity profile for the center-foot inclinometer (CFI), Springer Ranch Landslide.

In each inclinometer hole, the depth creep occurs in silty clay that is assumed to have the strength properties measured on core from the center-head inclinometer. These properties are an angle of internal friction of 15°, a cohesion of $8X10^2$ N/m^2, and a dry density of 1900 kg/m^3. The strength properties are based on consolidated drained direct shear tests on undisturbed weathered clay similar to that found in the zone of depth creep in the landslide. Also, for purposes of analysis the slope is taken to be an average of 10°. Finally, the piezometric level in each case is taken to be near the depth of the slide, an average of the observed levels.

For the center-head inclinometer (CHI, figs. 8 and 13) the slide thickness, h, is 4.85 m and h_p is taken to be 4 m. If these and the above values are substituted in equation 17, we arrive at the observed value of 1 m for x_2*, and if a viscosity of $2.55X10^{12}$ Ns/m^2 is assumed in equation 19, we have the observed average "plug" velocity of $2.2X10^{-10}$ m/s. The velocity distribution predicted by equation 20 is shown as a dotted line in figure 13.

The displacements and velocity distribution for the north-flank inclinometer (NFI) are shown in figures 9 and 14. The slide thickness is 4.8 m and h_p is taken to be 4 m. Substituting these and the values given above in equation 17, we find the predicted x_2* to be 1.27 m. The observed maximum velocity of $4.6X10^{-10}$ m/s is found if the Bingham viscosity here is $1.46X10^{12}$ Ns/m^2. The velocity predicted by equation 20 is again given by a dotted line.

Displacements and velocities for the center-middle inclinometer (CMI) are shown in figures 10 and 15. The slide thickness here is 2.9 m and h_p is assumed to be 2.6 m. Equation 17 predicts that x_2*=1 m, and equation 19 gives the maximum velocity, v_1*, of $4X10^{-10}$ m/s. The small differences between the observed and predicted velocity distributions (fig. 15) may be due to the presence of a step in the bottom topography of the slide near this inclinometer hole or due to the effect of inclinometer casing stiffness (see below).

Figures 11 and 16 show the displacement and velocity distributions for the south-flank inclinometer (SFI). The slide thickness here is 3.8 m and h_p is assumed to be 3.3 m. Equation 17 predicts that x_2* is 1.26 m, and equation 19 gives the maximum velocity of $3.0X10^{-10}$ m/s. Equation 20 (dotted line in fig. 16) gives a good fit to the velocities inferred from the displacements (fig. 11).

Figures 12 and 17 show the displacements and velocities for the center-foot inclinometer (CFI). Here the slide thickness is taken to be 5 m, and h_p is 4.0 m, which is close to observed piezometric levels. Equation 17 predicts that x_2* is 1.8 m, and the predicted maximum velocity, v_1*, is (equation 20) $4X10^{-10}$ m/s. Differences between the observed (solid line in fig. 17) and predicted (dotted line) velocity distributions appear to be due to the fact that the inclinometer data here are probably affected by casing stiffness and do not clearly indicate where the bottom of the slide occurs (see below).

The effect of casing stiffness can be seen by considering the deformation of an elastic member under the conditions shown in figure 18a. The resulting displacement profile (obtained by solving the "beam" equation

$$\frac{d^4u}{dx^4} = 0$$

subject to the boundary conditions shown in figure 18a) is

$$u = u_o \left[3\left(\frac{x}{a}\right)^2 - 2\left(\frac{x}{a}\right)^3\right] \qquad (21).$$

Equation 21 is plotted in figure 18b.

The effect of casing stiffness can be seen in figures 8 through 11 where bowing and negative displacements occur below the lower limit of creep movement. In figures 14, 15, and 17, differences between the observed and predicted velocity profiles can probably be accounted for by the stiffness of the casing.

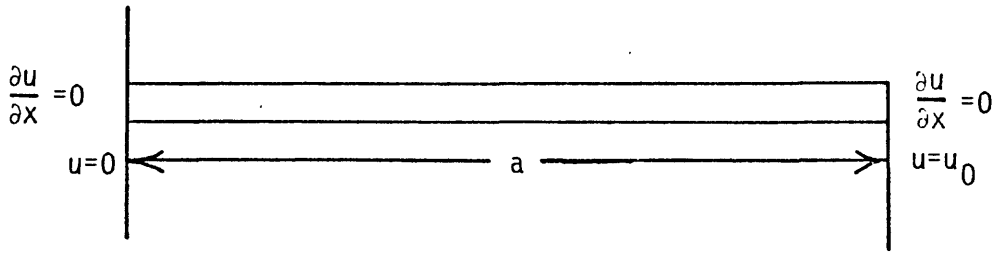

18a

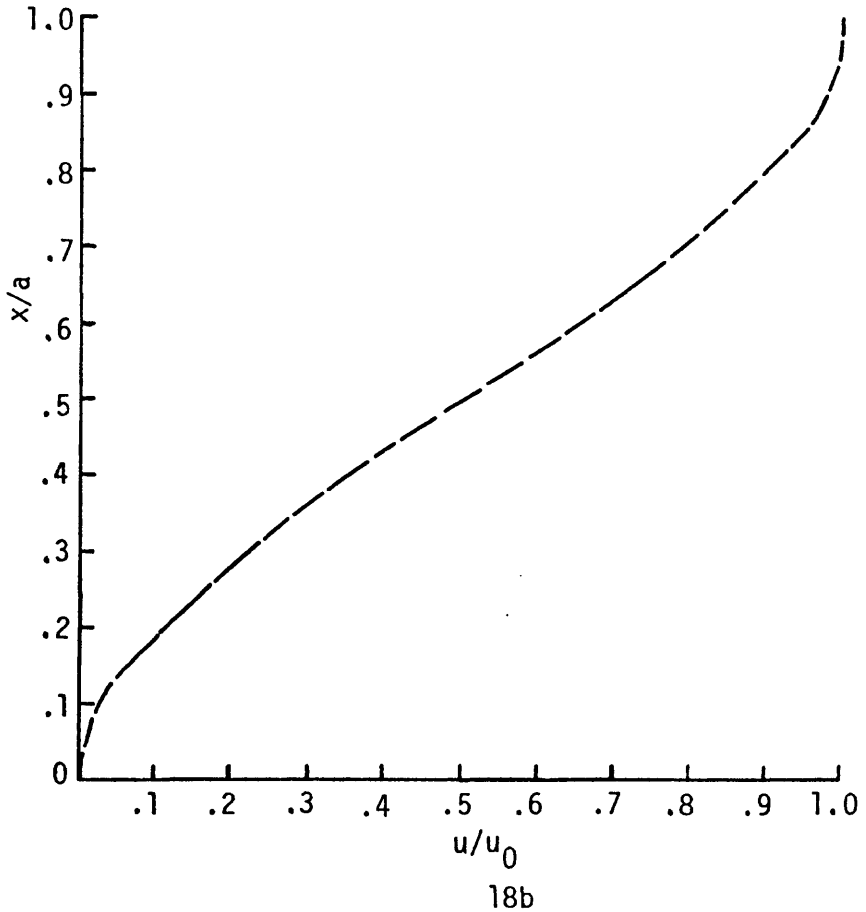

18b

Figure 18a and 18b.--Deformation of an elastic member of length "a" under conditions of no rotation and applied displacements of u=0 and u=u_0 at the ends.

Discussion

A number of points are worth reiteration here. We have seen in each case that the velocity within the zone of depth creep is parabolic and, aside from the effects of casing stiffness, reasonably well predicted by the theoretical results (equation 20). The thickness of zone of depth creep, x_2^*, can be found (equation 17) from quantities measured in the laboratory; dry density, ρ, and the strength parameters, α and k, and in the field; the total slide thickness, h, the slope angle, θ, the piezometric level, h_p, and the surcharge tractions C_n and C_s.

The Bingham viscosity, η_1, is more difficult to measure independently. However, because its only effect is on the magnitude of the velocity (equations 18 and 19), it can be easily "back calculated" (as was done above) provided field data is available.

It is interesting to compare viscosities computed in this way with the viscosity values for clays from various sources compiled by Yen (1969). The average of these values, 1.30×10^{12} Ns/m^2, is somewhat lower than the average viscosities computed for the Springer Ranch slide, 2.14×10^{12} Ns/m^2. However, the Springer Ranch data are close to the laboratory determinations of Geuze and Tan (1953) of 2.63×10^{12} Ns/m^2.

Also, all the "back-calculated viscosities are based on the assumption that the creeping flow is continuous over the period of observation. This is usually not true, as landslide movement is episodic and most movement occurs during especially wet periods when the piezometric level is high. If, for example, most slide movement occurs over periods of less than 1 day, the velocities would be higher and the viscosities lower by two to three orders of magnitude. Such movements are likely to be ignored unless continuous monitoring systems are installed.

References

Chleborad, A. F., 1980, Investigation of a natural slope failure in weathered Tertiary deposits western Powder River Basin, Wyoming: U.S. Geological Survey Open-File Report 80-673, 66 p.

Corp, E. L., Schuster, R. L., and McDonald, M. M., 1975, Elastic-plastic stability analysis of mine-waste embankments: U.S. Bureau of Mines Report of Investigations 8069, 98 p.

Drucker, D. C., and Prager, W., 1952, Soil mechanics and plastic analysis or limit design: Quarterly Applied Mathematics, v. 10, p. 157-165.

Geuze, E. C. W. A., and Tan, T. K., 1953, Laboratory investigation, including compaction tests, improvement of soil properties: International Conference on Soil Mechanics and Foundation Engineering, 3d, Switzerland, 1953, Proceedings, v. 3, p. 121.

Gould, J. P., 1960, A study of shear failure in certain Tertiary marine sediments, in Research conference on shear strength of cohesive soils, Boulder, Colorado, June 1960: American Society of Civil Engineers, Soil Mechanics and Foundation Division, p. 615.

Oldroyd, J. G., 1947, Two-dimensional plastic flow of a Bingham solid--A plastic boundary layer theory for slow motion: Cambridge Philosophical Society Proceedings, v. 43, p. 383-395.

Olszak, W., and Perzyna, P., 1966, On elastic/visco-plastic soils, in Kravtchenko, J., and Sirieys, P. M., Rheology and soil mechanics: International Union of Theoretical and Applied Mathematics [IUTAM], Proceedings, Grenoble, 1964, p. 47-57.

Ter-Stepanian, G., 1963, On the long-term stability of slopes: Norwegian Geotechnical Institute Publication 52, p. 1-13.

_____1965, In-situ determination of the rheological characteristics of soils on slopes: International Conference on Soil Mechanics and Foundation Engineering, 6th, Montreal, 1965, Proceedings, v. 2, p. 575-577.

Yen, B. C., 1969, Stability of slopes undergoing creep deformation: American Society of Civil Engineers Proceedings, v. 95, p. 1075-1096.